

# In Situ Synthesis of FeSn<sub>2</sub>/Graphene Nanocomposite via One-Pot Solvothermal Route and Its Electrochemical Li-Storage Properties

Bin Feng, Jian Xie, Gao-Shao Cao<sup>\*</sup>, Tie-Jun Zhu, and Xin-Bing Zhao

State Key Laboratory of Silicon Materials and Department of Materials Science and Engineering, Zhejiang University, Hangzhou 310027, China

\*E-mail: [gscao@zju.edu.cn](mailto:gscao@zju.edu.cn)

Received: 3 May 2012 / Accepted: 19 May 2012 / Published: 1 June 2012

---

In this work, a FeSn<sub>2</sub>/graphene nanocomposite was synthesized by a facile in situ one-pot solvothermal route. X-ray diffraction (XRD), X-ray photoelectron spectroscopy (XPS) and Raman spectra (RS) results indicated that the formation of FeSn<sub>2</sub> and the reduction of graphite oxide (GO) to graphene occur simultaneously during the one-pot solvothermal process. Scanning electron microscopy (SEM) and transmission electron microscopy (TEM) observations showed that the quasi-spheric FeSn<sub>2</sub> particles with a size of 10–30 nm are uniformly anchored on graphene. The electrochemical Li-storage performance of the nanocomposite was investigated by galvanostatic cycling. The nanocomposite exhibits an obvious improved electrochemical performance compared to bare FeSn<sub>2</sub>. The enhancement of the electrochemical performance could be attributed to the introduction of graphene that not only constructs two-dimensional conductive networks but also disperses and confines the FeSn<sub>2</sub> nanoparticles.

---

**Keywords:** graphene, FeSn<sub>2</sub>, nanocomposite, anode material, electrochemical performance

## 1. INTRODUCTION

In recent years, the investigation of high-capacity anodes to replace carbonaceous materials for Li-ion batteries has received a great interest due to the increasing demand for high energy density of Li-ion batteries. Among them, Sn-based alloys are attractive because metallic tin can react with lithium to yield a high theoretical capacity of 993 mAh g<sup>-1</sup> [1-3]. However, metallic tin undergoes large volume changes during the discharge and charge processes which cause a rapid capacity fading [3, 4]. In order to improve the cycle life, M-Sn alloys, where M is a transition metal, have been proposed to

replace metallic tin [5–10]. The electrochemical inactive metallic particles M are expected to buffer the volume variations and limit the coalescence of tin particles during the electrochemical cycling. FeSn<sub>2</sub> is a typical Sn alloy, which showed a large first reversible capacity and relatively low Li-storage voltage [11]. However, this material also exhibited poor cycling performance. To improve its cycling performance, some strategies were suggested, such as using nanosized particles [12, 13] or dispersing the particles on a matrix [14, 15]. Among various matrices, carbon materials have been regarded as the best choice because they not only contribute to the overall capacity but also enhance the electrical conductivity, in addition to the dispersing and buffering effect.

Graphene, a flat monolayer of sp<sup>2</sup>-bonded carbon atoms arranged in a tightly packed honeycomb two-dimensional (2D) lattice, has received considerable attention since first discovered by K. S. Novoselov et al [16]. It exhibits high electronic conductivity [17], high specific surface area [18] and high mechanical strength [19], which makes it a promising 2D support or building block for constructing functional nanocomposites. Recently, the research on some Si or Sn-based metals [20-22], oxides [23-25] and alloys [26, 27] has shown that the electrochemical performance of these materials can be greatly enhanced by loading them onto graphene. The flexible graphene not only acts as a buffer to relieve the large volume changes during Li-absorption/extraction processes but also as a separator to block the aggregation of the nanoparticles upon repeated cycling.

In this work, we report the preparation of FeSn<sub>2</sub>/graphene (FeSn<sub>2</sub>/G) nanocomposite by a facile in situ one-pot solvothermal route. The electrochemical tests showed that the FeSn<sub>2</sub>/graphene nanocomposite exhibits an improved electrochemical performance compared with bare FeSn<sub>2</sub>, indicating a potential application as anode for Li-ion batteries.

## 2. EXPERIMENTAL SECTION

### 2.1 Synthesis of FeSn<sub>2</sub>/G nanocomposite

For the preparation of the FeSn<sub>2</sub>/G nanocomposite, graphite oxide (58.6 mg), synthesized by the modified Hummer's method [28], was ultrasonically dispersed in 60 mL of absolute ethanol for 3 h to get exfoliated graphene oxide using an ultrasonic bath (KQ5200B). Subsequently, 1 mmol of FeCl<sub>3</sub>·6H<sub>2</sub>O and 2 mmol of SnCl<sub>2</sub>·2H<sub>2</sub>O were added to the above solution. After sonication for another 0.5 h, sufficient NaBH<sub>4</sub> was slowly added to the mixed solution to reduce Fe<sup>3+</sup> and Sn<sup>2+</sup> to metallic Fe and Sn. The mixture was transferred to a Teflon-lined stainless steel autoclave (80 mL) and heated at 220 °C for 24 h in an electric oven. During the solvothermal process, Fe and Sn were converted into FeSn<sub>2</sub> [13] and graphite oxide was reduced to graphene by NaBH<sub>4</sub> [29]. The resultant product was separated by centrifugation, washed with deionized water and dried at 40 °C under vacuum overnight. The bare FeSn<sub>2</sub> was prepared using the similar process for comparison without adding graphite oxide.

### 2.2 Materials Characterizations

The crystalline structures of the products were characterized by X-ray diffraction (XRD) on a Rigaku D/Max-2550pc powder diffractometer equipped with Cu K<sub>α</sub> radiation ( $\lambda = 1.54 \text{ \AA}$ ). The

morphologies of the products were observed by field emission scanning electron microscopy (SEM) on a FEI-sirion microscope, transmission electron microscopy (TEM) and high-resolution TEM (HRTEM) on a JEM 2100F microscope. X-ray photoelectron spectroscopy (XPS) measurements were performed on a KRATOS AXIS ULTRA-DLD spectrometer with a monochromatic Al K $\alpha$  radiation ( $h\nu = 1486.6$  eV). Raman spectra were recorded on a Jobin-Yvon Labor Raman HR-800 Raman system by exciting a 514.5 nm Ar $^+$  laser. The carbon content analysis was conducted on a Flash EA 1112 tester.

### 2.3 Electrochemical measurements

The electrochemical properties of the active materials (FeSn $_2$ /G, bare FeSn $_2$ ) were evaluated with coin cells (CR 2025). The slurry was made by dispersing active material, acetylene black and polyvinylidene fluoride (PVDF) (75:15:10 in weight) in N-methyl pyrrolidone (NMP) under magnetic stirring. The working electrodes were made by coating the slurry onto Ni foam. After drying at 100 °C under vacuum for 8 h, the working electrodes were assembled into half cells in an argon-filled glove box using metallic Li foil as the counter electrode, 1 M LiPF $_6$  in ethylene carbonate (EC)-dimethyl carbonate (DMC) (1:1 in volume) as the electrolyte, and polypropylene micro-porous film (Celgard 2300) as the separator. The cells were galvanostatically cycled on a LHS-B-5V10mA8D battery tester in the voltage range of 0.05–2 V (vs. Li/Li $^+$ ) at various current densities. For the FeSn $_2$ /G composite, the specific capacity (mAh g $^{-1}$ ) values are referred to the masses of both FeSn $_2$  and graphene. Cyclic voltammetry (CV) measurements were performed on an Arbin BT2000 system between 0.05 and 2 V (vs. Li/Li $^+$ ) at 0.1 mV s $^{-1}$ . Electrochemical impedance spectroscopy (EIS) measurements were carried out on a CHI660C electrochemical workstation using two-electrode coin cells. The impedance spectra were recorded by applying an ac signal of 5 mV amplitude over the frequency range from 10 $^{-2}$  Hz to 10 $^5$  Hz at de-lithiation state. All of the electrochemical measurements were conducted at room temperature.

## 3. RESULTS AND DISCUSSION

Fig. 1 shows the XRD patterns of the FeSn $_2$ /G composite and bare FeSn $_2$ . The dominant diffraction peaks of both samples can be indexed to FeSn $_2$  (space group  $I4/mcm$ , JCPDS No. 25-0415). Minor FeSn diffraction peaks are also observed for both samples. Note that the diffraction peaks related to graphene cannot be detected; indicative of that the restacking of the graphene sheets after reduction was inhibited by uniformly loading FeSn $_2$  nanoparticles in between the graphene sheets. The content of graphene is estimated to be 5.8 wt. % by carbon content analysis.

Fig. 2(a) shows the SEM image of a FeSn $_2$ /G flake. Through the transparent graphene, it is clear that nanosized FeSn $_2$  particles are uniformly confined in between the graphene sheets. A layered structure with alternating FeSn $_2$  nanoparticles and graphene sheet is evident from the broken cross

section of the flake (denoted by the arrows). However, without the confinement by graphene, the FeSn<sub>2</sub> nanoparticles at the surface of the graphene tend to aggregate.

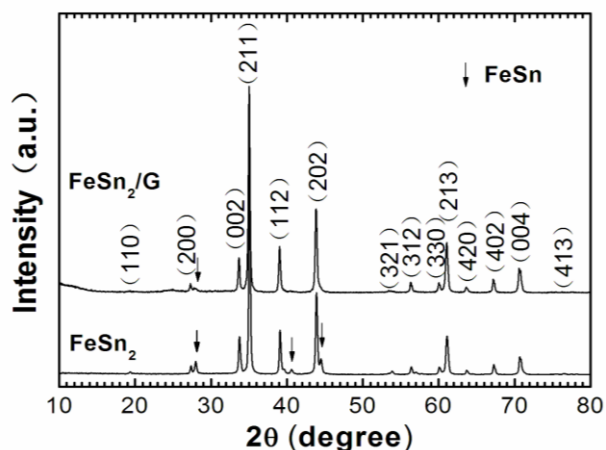


Figure 1. XRD patterns of FeSn<sub>2</sub>/G and bare FeSn<sub>2</sub>.

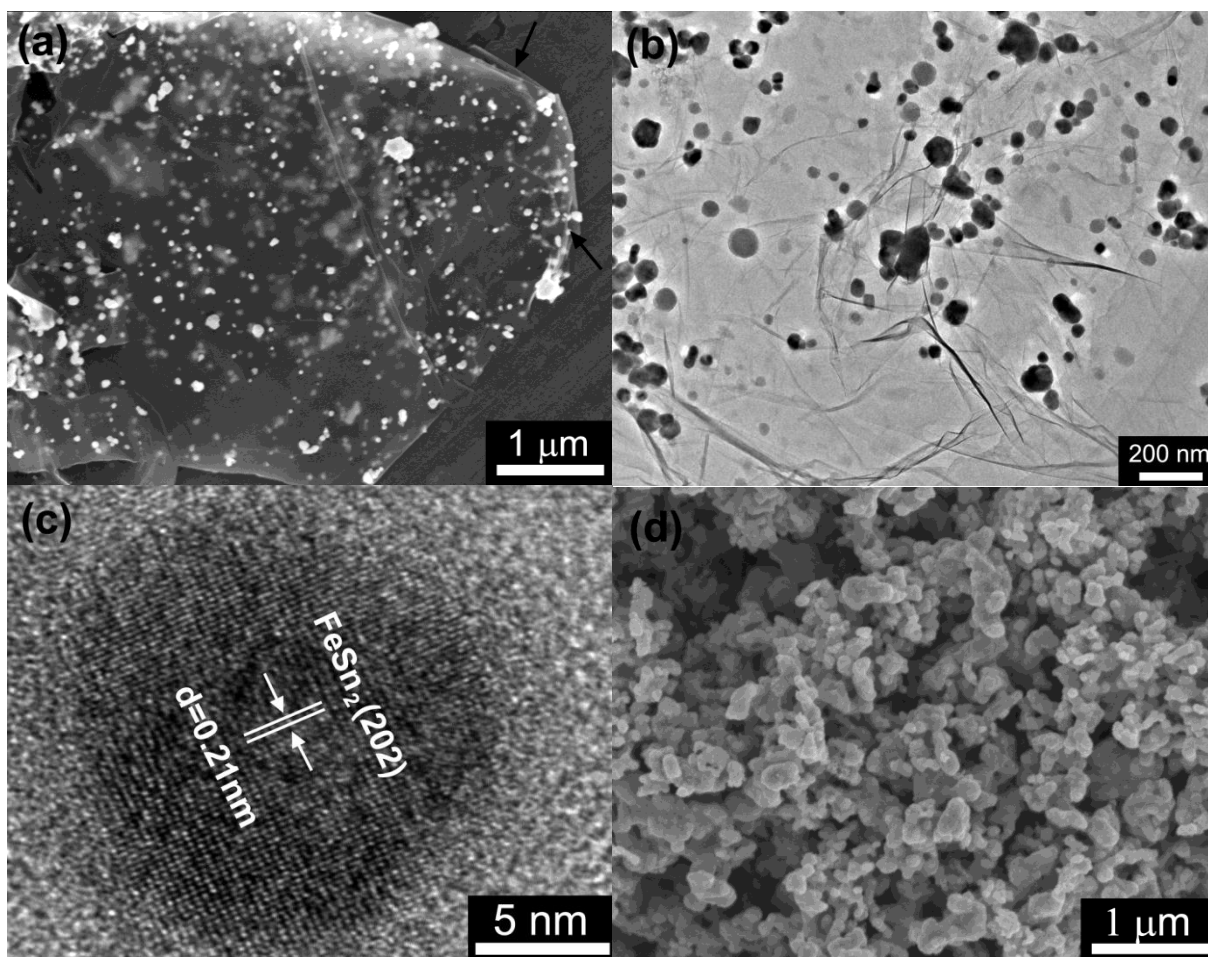
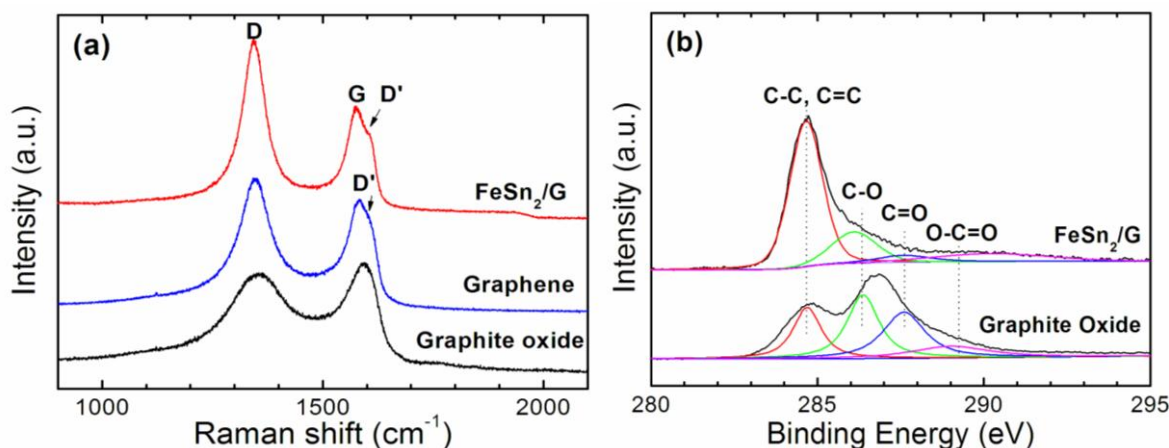


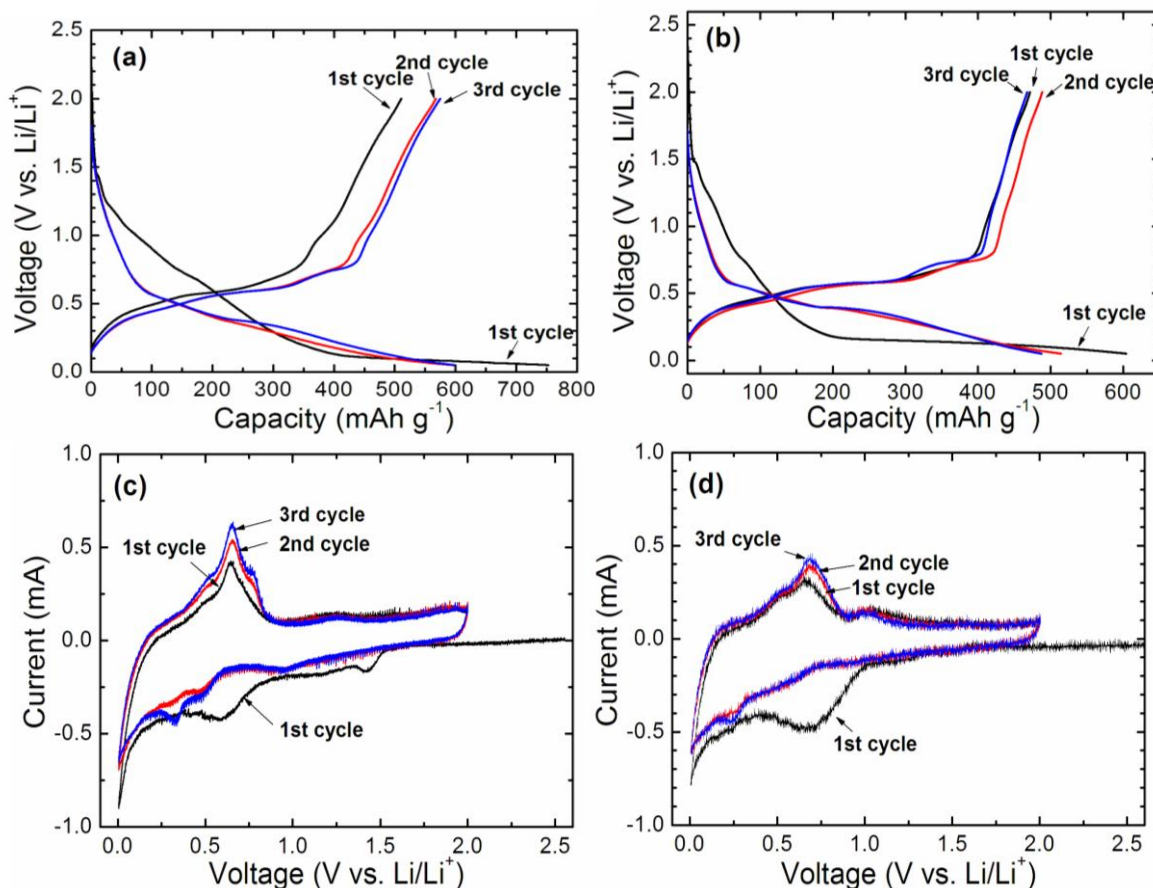
Figure 2. (a) SEM, (b) TEM, (c) HRTEM images of FeSn<sub>2</sub>/G, and (d) SEM images of bare FeSn<sub>2</sub>.

TEM image in Fig. 2(b) indicates that the graphene is decorated uniformly by the  $\text{FeSn}_2$  particles with a size of 10–30 nm. The graphene is rather thin evidenced by its transparent nature and the surface wrinkles. Fig. 2(c) demonstrates the lattice resolved HRTEM image of an individual  $\text{FeSn}_2$  particle anchored on graphene. The fringe spacing is measured to be 0.21 nm, related to the interplanar spacing of (202) plane of  $\text{FeSn}_2$ . For comparison, the SEM image of bare  $\text{FeSn}_2$  is also presented as seen in Fig 2(d). Note that, without the confinement by graphene, the  $\text{FeSn}_2$  nanoparticles tend to aggregate and have larger particle sizes in the range of 100 to 200 nm.



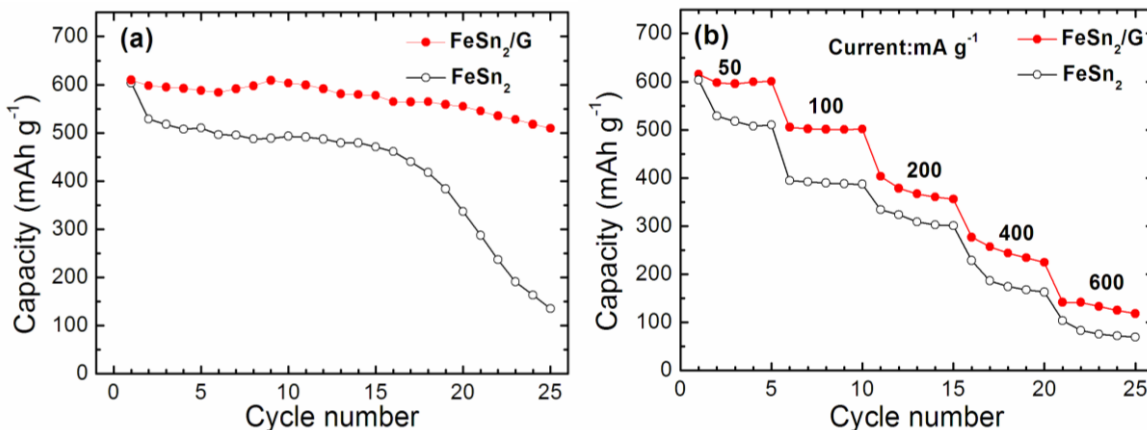
**Figure 3.** (a) Raman spectra of  $\text{FeSn}_2/\text{G}$ , graphene and graphite oxide and (b) C 1s XPS of  $\text{FeSn}_2/\text{G}$  and graphite oxide.

Fig. 3(a) gives the Raman spectra of  $\text{FeSn}_2/\text{G}$ , graphene and graphite oxide. For all the three samples, two bands at 1350 and 1580  $\text{cm}^{-1}$  appear, corresponding to the disordered (D) and graphitic (G) bands of carbon-based materials [30]. Compared with graphite oxide, both  $\text{FeSn}_2/\text{G}$  and graphene exhibit an increased D/G intensity ratio, which is caused by a reduction of the average size of the  $\text{sp}^2$  domains and an increased number of these domains, indicating the reduction of graphite oxide to graphene [31]. It should be addressed that the G peak shows an asymmetric feature. It is actually composed of two overlapping peaks, G and D', located at 1580 and 1620  $\text{cm}^{-1}$ , respectively. The D' peak is a defect peak due to intra-valley scattering [30]. The asymmetric feature of G peak of graphene was also observed in other work [32, 33]. Fig. 3(b) presents the C 1s XPS of  $\text{FeSn}_2/\text{G}$  and graphite oxide. The XPS is fitted into four peaks, corresponding to carbon atoms in four functional groups: non-oxygenated carbon (C-C 285.6 eV or C=C 284.8 eV), carbon in C-O group (epoxide or hydroxyl, 286.3 eV), carbonyl carbon (C=O, 287.6 eV) and carboxylate carbon (O-C=O, 289.0 eV) [29, 31, 34]. Note that the peak intensity of carbons in C-O, C=O and O-C=O groups exhibits a significant decrease in  $\text{FeSn}_2/\text{G}$  compared with that in graphite oxide, indicative of a remarkable reduction of graphite oxide into graphene after the solvothermal reaction. It should be noted that the solvothermal products still contain residual epoxide and/or hydroxyl groups, in consistent with the theoretical calculation that these groups are difficult to remove when located at the edges of the graphite oxide [35].



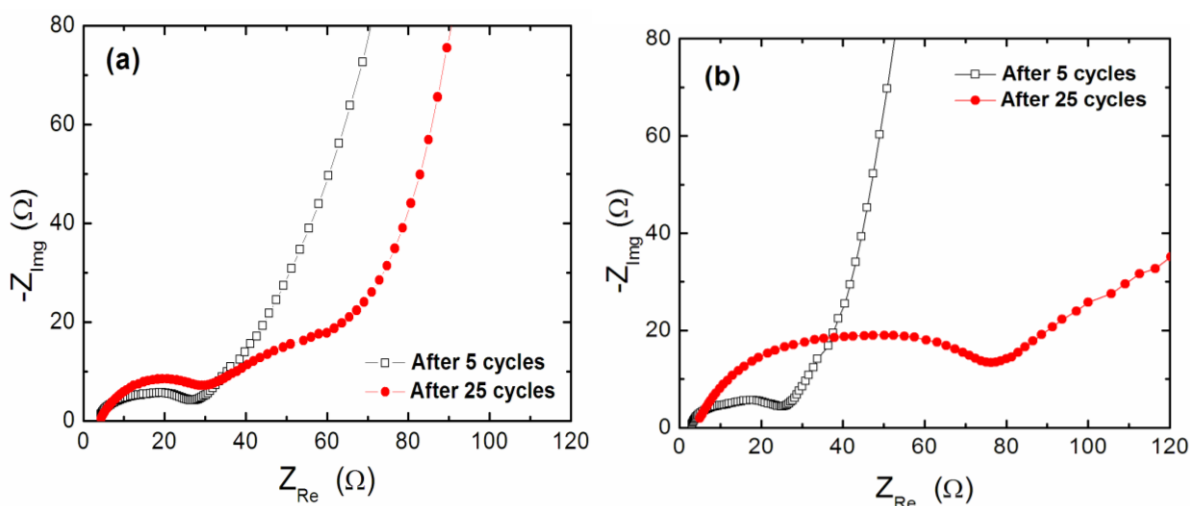
**Figure 4.** (a) charge-discharge curves ( $50 \text{ mA g}^{-1}$ ) of  $\text{FeSn}_2/\text{G}$ , (b) charge-discharge curves ( $50 \text{ mA g}^{-1}$ ) of bare  $\text{FeSn}_2$ , (c) CV plots at  $0.1 \text{ mV s}^{-1}$  of  $\text{FeSn}_2/\text{G}$  and (d) CV plots at  $0.1 \text{ mV s}^{-1}$  of bare  $\text{FeSn}_2$ .

Fig. 4(a) shows the charge-discharge curves of  $\text{FeSn}_2/\text{G}$  for the first three cycles. The nanocomposite gives a first discharge (Li-absorption) capacity of  $752 \text{ mAh g}^{-1}$  and a first charge (Li-extraction) capacity of  $510 \text{ mAh g}^{-1}$ . The large first irreversible capacity can be attributed to the reduction decomposition of the electrolyte and the formation of the solid electrolyte interface (SEI) layer. In addition, the surface oxide also contributes to part of the irreversible capacity. After the first cycle, reversible electrochemical reactions take place evidenced by the almost overlapped charge or discharge curves. For comparison, the charge-discharge curves of bare  $\text{FeSn}_2$  for the first three cycles are shown in Fig. 4(b). The electrochemical reaction mechanism of the  $\text{FeSn}_2/\text{G}$  nanocomposite was investigated by CV shown in Fig. 4(c). During the first scan, a reduction peak appears at about  $0.6 \text{ V}$ , corresponding to the quasi-plateau in the first discharge curve, which is related to the formation of the SEI layer. After the first scan, the reduction and oxidation peaks are fixed at around  $0.3$  and  $0.7 \text{ V}$ , respectively, suggesting a good reversibility during the subsequent cycling. CV plots of bare  $\text{FeSn}_2$  for the first three cycles are also shown in Fig 4(d) for comparison. Note that the oxidation peak of  $\text{FeSn}_2/\text{G}$  is sharper than that of bare  $\text{FeSn}_2$ , indicating better electrode kinetics due to the introduction of conductive graphene.



**Figure 5.** (a) cycling stability at 50 mA g<sup>-1</sup> and (b) rate capability between FeSn<sub>2</sub>/G and bare FeSn<sub>2</sub>.

Fig. 5(a) compares the cycling stability between FeSn<sub>2</sub>/G and bare FeSn<sub>2</sub>. Obviously, the nanocomposite exhibits an improved cycling stability compared to bare FeSn<sub>2</sub>. After 25 cycles, a capacity close to 500 mAh g<sup>-1</sup> is maintained for FeSn<sub>2</sub>/G, while for bare FeSn<sub>2</sub>, the capacity drops rapidly to 150 mAh g<sup>-1</sup> after the same cycles. The enhanced cycling stability is attributed to the buffering effect of graphene that alleviates the large volume changes and the confining effect of graphene that refrains the aggregating of the FeSn<sub>2</sub> nanoparticles. Fig. 5(b) compares the rate capability between FeSn<sub>2</sub>/G and bare FeSn<sub>2</sub>. Apparently, FeSn<sub>2</sub>/G also shows a better rate capability than bare FeSn<sub>2</sub>. The improvement in rate capability originates mainly from the following factors: first, the highly conductive graphene offers a 2D conducting channel for the FeSn<sub>2</sub> nanoparticles; second, small-sized, well-dispersed nanoparticles facilitates rapid Li-ion transport; third, the layered structure is beneficial for better wetting of the active material by the electrolyte, thus enabling faster Li-ion transport through the electrolyte/electrolyte interface.



**Figure 6.** Impedance plots of (a) the FeSn<sub>2</sub>/G and (b) bare FeSn<sub>2</sub> after 5 and 25 cycles.

Fig. 6(a) gives the Nyquist plots of FeSn<sub>2</sub>/G and bare FeSn<sub>2</sub> after 5 and 25 cycles. The Nyquist plots are composed of two partially overlapped semicircles at high- and medium-frequency ranges and a slopping line in the low frequency region. As previously reported [36], the first semicircle is correlated to Li-ions transport resistance through the SEI layer ( $R_{SEI}$ ), the second one corresponds to the charge transfer resistance ( $R_{ct}$ ), the slopping line is related to the Li-ion diffusion in the bulk material, and the intercept on the  $Z'$  axis at high frequency is related to the electrolyte resistance ( $R_e$ ). For the FeSn<sub>2</sub>/G electrode,  $R_{SEI}$  keeps almost unchanged after 5 and 25 cycles (Fig. 6(a)), indicating that the microstructure of the SEI layer is stabilized after the initial cycles. The stabilized SEI layer can prevent the direct exposure of the active material to the electrolyte, blocking the further reduction decomposition of the electrolyte, which is favorable for the stable and reversible cycling of the electrode. For the bare FeSn<sub>2</sub> electrode, however, both  $R_{SEI}$  and  $R_{ct}$  show an apparent increase during cycling (Fig. 6(b)). An obvious increase in  $R_e$  is also observed for the bare FeSn<sub>2</sub> electrode during cycling, caused possibly by the exfoliation of the active material into the electrolyte. On the contrary, the FeSn<sub>2</sub>/G electrode exhibits a minor change in  $R_e$ , implying that the exfoliation of the active material is slight due to the buffering effect of graphene. This can also explain the better cycling stability of the FeSn<sub>2</sub>/G electrode. As a result, the EIS tests agree well with electrochemical properties.

#### 4. CONCLUSIONS

In summary, FeSn<sub>2</sub>/G nanocomposite has been synthesized by a simple in situ one-pot solvothermal route. FeSn<sub>2</sub> nanoparticles are uniformly anchored on the graphene, forming a unique layered nanostructure. FeSn<sub>2</sub>/G shows an improved cycling stability compared to the bare FeSn<sub>2</sub>. The improvement in cycling stability is attributed to the incorporation of the flexible graphene that acts both as a buffer to alleviate the volume changes and as a separator to hinder the aggregation of nanoscaled particles. In addition, the introduction of the graphene also offers a 2D conductive network and uniformly disperses the alloy nanoparticles, leading to enhanced electrochemical reaction kinetics. The results clearly indicate graphene plays a crucial role in the improved electrochemical performance of the nanosized FeSn<sub>2</sub> alloys with potential application as anode in Li-ion batteries.

#### ACKNOWLEDGEMENTS

This work was supported by the National Natural Science Foundation of China (No. 51101139), the Ph.D. Programs Foundation of Ministry of Education of China (No. 20100101120024), the Foundation of Education Office of Zhejiang Province (No. Y201016484), the Qianjiang Talents Project of Science Technology Department of Zhejiang Province (2011R10021), Key Science and Technology Innovation Team of Zhejiang Province under grant number 2010R50013.

#### References

1. J. Hassoun, G. Derrien, S. Panero, and B. Scrosati, *Adv. Mater.*, 20 (2008) 3169.
2. G. Derrien, J. Hassoun, S. Panero, and B. Scrosati, *Adv. Mater.*, 19 (2007) 2336.
3. M. Winter and J. O. Besenhard, *Electrochim. Acta*, 45 (1999) 31.
4. J. H. Kim, G. J. Jeong, Y. W. Kim, H. J. Sohn, C. W. Park, and C. K. Lee, *J. Electrochem. Soc.*, 150 (2003) A1544.

5. X. L. Wang, W. Q. Han, J. Chen, and J. Graetz, *ACS Appl. Mater. Interfaces*, 2 (2010) 1548.
6. M. M. Thackeray, J. T. Vaughey, A. J. Kahaian, K. D. Kepler, and R. Benedek, *Electrochem. Commun.*, 1 (1999) 111.
7. O. Mao, R. L. Turner, I. A. Courtney, B. D. Fredericksen, M. I. Buckett, L. J. Krause, and J. R. Dahn, *Electrochem. Solid State Lett.*, 2 (1999) 3.
8. S. Naille, C. M. Ionica-Bousquet, F. Robert, F. Morato, P. E. Lippens, and J. Olivier Fourcade, *J. Power Sources*, 174 (2007) 1091.
9. H. Groult, H. El Ghallali, A. Barhoun, E. Briot, C. M. Julien, F. Lantelme, and S. Borensztjan, *Electrochim. Acta*, 56 (2011) 2656.
10. J. Hassoun, G. A. Elia, S. Panero, and B. Scrosati, *J. Power Sources*, 196 (2011) 7767.
11. O. Mao, R. A. Dunlap, and J. R. Dahn, *J. Electrochem. Soc.*, 146 (1999) 405.
12. M. Chamas, P. E. Lippens, J. C. Jumas, K. Boukerma, R. Dedryvère, D. Gonbeau, J. Hassoun, S. Panero, and B. Scrosati, *J. Power Sources*, 196 (2011) 7011.
13. C. Q. Zhang, J. P. Tu, X. H. Huang, Y. F. Yuan, S. F. Wang, and F. Mao, *J. Alloy. Compd.*, 457 (2008) 81.
14. U. G. Nwokeke, F. Nacimiento, R. Alcantara, and J. L. Tirado, *Electrochem. Solid State Lett.*, 14 (2011) A148.
15. S. Yoon, J. M. Lee, H. Kim, D. Im, S. G. Doo, and H. J. Sohn, *Electrochim. Acta*, 54 (2009) 2699.
16. K. S. Novoselov, A. K. Geim, S. V. Morozov, D. Jiang, Y. Zhang, S. V. Dubonos, I. V. Grigorieva, and A. A. Firsov, *Science*, 306 (2004) 666.
17. S. Park, J. An, I. Jung, R. D. Piner, S. J. An, X. Li, A. Velamakanni, and R. S. Ruoff, *Nano Lett.*, 9 (2009) 1593.
18. M. D. Stoller, S. Park, Y. Zhu, J. An, and R. S. Ruoff, *Nano Lett.*, 8 (2008) 3498.
19. C. Lee, X. Wei, J. W. Kysar, and J. Hone, *Science*, 321 (2008) 385.
20. G. Wang, B. Wang, X. Wang, J. Park, S. Dou, H. Ahn, and K. Kim, *J. Mater. Chem.*, 19 (2009) 8378.
21. J. K. Lee, K. B. Smith, C. M. Hayner, and H. H. Kung, *Chem. Commun.*, 46 (2010) 2025.
22. J. Z. Wang, C. Zhong, S. L. Chou, and H. K. Liu, *Electrochem. Commun.*, 12 (2010) 1467.
23. J. Yao, X. Shen, B. Wang, H. Liu, and G. Wang, *Electrochem. Commun.*, 11 (2009) 1849.
24. S. M. Paek, E. Yoo, and I. Honma, *Nano Lett.*, 9 (2008) 72.
25. L. S. Zhang, L. Y. Jiang, H. J. Yan, W. D. Wang, W. Wang, W. G. Song, Y.-G. Guo, and L. J. Wan, *J. Mater. Chem.*, 20 (2010) 5462.
26. S. Chen, P. Chen, M. Wu, D. Pan, and Y. Wang, *Electrochem. Commun.*, 12 (2010) 1302.
27. Y. Zheng, J. Xie, S. Liu, W. Song, G. Cao, T. Zhu, and X. Zhao, *J. Power Sources*, 202 (2012) 276.
28. W. S. Hummers and R. E. Offeman, *J. Am. Chem. Soc.*, 80 (1958) 1339.
29. H. J. Shin, K. K. Kim, A. Benayad, S. M. Yoon, H. K. Park, I. S. Jung, M. H. Jin, H. K. Jeong, J. M. Kim, J. Y. Choi, and Y. H. Lee, *Adv. Funct. Mater.*, 19 (2009) 1987.
30. A. C. Ferrari, *Solid State Commun.* 143 (2007) 47.
31. S. Stankovich, D. A. Dikin, R. D. Piner, K. A. Kohlhaas, A. Kleinhammes, Y. Jia, Y. Wu, S. T. Nguyen, and R. S. Ruoff, *Carbon*, 45 (2007) 1558.
32. G. Wang, J. Yang, J. Park, X. Gou, B. Wang, H. Liu, and J. Yao, *J. Phys. Chem. C*, 112 (2008) 8192.
33. H. Wang, J. T. Robinson, X. Li, and H. Dai, *J. Am. Chem. Soc.*, 131 (2009) 9910.
34. S. Stankovich, R. D. Piner, X. Chen, N. Wu, S. T. Nguyen, and R. S. Ruoff, *J. Mater. Chem.*, 16 (2006) 155.
35. X. F. Guo, J. Jang, and S. Nagase, *J. Phys. Chem. C*, 114 (2010) 832.
36. D. Aurbach, *J. Power Sources*, 89 (2000) 206.